Event-by-event study of prompt neutrons from 239Pu(n,f)

R. Vogt, J. Randrup, J. Pruet, W. Younes

July 29, 2009

Disclaimer

This document was prepared as an account of work sponsored by an agency of the United States government. Neither the United States government nor Lawrence Livermore National Security, LLC, nor any of their employees makes any warranty, expressed or implied, or assumes any legal liability or responsibility for the accuracy, completeness, or usefulness of any information, apparatus, product, or process disclosed, or represents that its use would not infringe privately owned rights. Reference herein to any specific commercial product, process, or service by trade name, trademark, manufacturer, or otherwise does not necessarily constitute or imply its endorsement, recommendation, or favoring by the United States government or Lawrence Livermore National Security, LLC. The views and opinions of authors expressed herein do not necessarily state or reflect those of the United States government or Lawrence Livermore National Security, LLC, and shall not be used for advertising or product endorsement purposes.

Event-by-event study of prompt neutrons from ^{239}Pu(n, f)

R. Vogt[1,2], J. Randrup[3], J. Pruet[1], and W. Younes[1]

[1] *Physics Division, Lawrence Livermore National Laboratory, Livermore, CA 94551, USA*
[2] *Physics Department, University of California, Davis, CA 95616, USA*
[3] *Nuclear Science Division, Lawrence Berkeley National Laboratory, Berkeley, CA 94720, USA*
(Dated: July 28, 2009)

Employing a recently developed Monte-Carlo model, we study the fission of ^{240}Pu induced by neutrons with energies from thermal to just below the threshold for second chance fission. Current measurements of the mean number of prompt neutrons emitted in fission, together with less accurate measurements of the neutron energy spectra, place remarkably fine constraints on predictions of microscopic calculations. In particular, the total excitation energy of the nascent fragments must be specified to within 1 MeV to avoid disagreement with measurements of the mean neutron multiplicity. The combination of the Monte-Carlo fission model with a statistical likelihood analysis also presents a powerful tool for the evaluation of fission neutron data. Of particular importance is the the fission spectrum, which plays a key role in determining reactor criticality. We show that our approach can be used to develop an estimate of the fission spectrum with uncertainties several times smaller than current experimental uncertainties for outgoing neutron energies of less than 2 MeV.

I. INTRODUCTION

The quest for a fundamental theory of fission began with the 1939 seminal work of Bohr and Wheeler [1], the same year as this phenomenon was discovered by Hahn and Strassmann [2] and interpreted by Meitner and Frisch [3]. Bohr and Wheeler used the liquid-drop model to make predictions that were remarkably realistic given the paucity of available data. The current theoretical descriptions of fission reflect the complexity and richness revealed over 70 years of experimental studies, emphasizing the multi-dimensional, dynamic, and microscopic aspects. In particular, a refined version of the liquid drop model that includes a finite interaction range and quantum shell corrections has formed the basis for extensive calculations of the potential-energy surfaces associated with the multidimensional shape of fissioning nuclei (see Refs. [4, 5] and references therein). Concurrently, a program is underway to develop a fully microscopic treatment of fission in terms of a quantum many-body treatment of protons and neutrons subject to an adjustable effective (in-medium) interaction [6–8].

Despite the many theoretical advances, there is not yet a quantitative theory of fission. This is unfortunate because nuclear fission remains important to society at large due to its many practical applications, including energy production and security. For example, reactors and other critical systems demand that neutron growth be known to about the 0.1% level for model simulations to be reliable. In such cases, scattering experiments are insufficiently accurate, requiring reliance on more inclusive, higher statistics integral critical assembly experiments.

Furthermore, in the last few years efforts have been underway to develop systems capable of detecting concealed nuclear material. These applications place entirely different demands on fission models by attempting to exploit specific information carried by particles resulting from fission. Thus there is a need for a fission description that accounts for particle correlations and fluctuations on an event-by-event level. Such a description, employing a model incorporating the relevant physics with a few key parameters, compared to the pertinent data through a statistical analysis, presents a potentially powerful tool for bridging the gap between current microscopic models and important fission observables and for improving estimates of the relatively gross fission characteristics important for applications. This type of approach also provides a means of using readily measured observables to constrain our understanding of the microscopic details of fission.

Relatively recently, Lemaire *et al.* [9] implemented a Monte-Carlo simulation of fission fragment statistical decay by sequential neutron emission for spontaneous fission of ^{252}Cf and thermal fission of ^{235}U. That work demonstrated how fission event simulations, in conjunction with experimental data on fission neutrons and physics models of fission and neutron emission, can be used to predict the neutron spectrum and to validate and improve the underlying physics models.

In the present work, we have implemented a conceptually similar approach and applied it to calculate the sequential neutron emission for the neutron induced fission of ^{240}Pu. Specifically, we have adapted the recently developed fission event generation model FREYA [29] to calculate the production and decay of fission fragments and used maximum-likelihood analysis to estimate properties of the emitted fission neutrons and their correlation coefficients. To our knowledge, such correlations have not been extracted before for fission neutrons in a physics-based Monte-Carlo simulation. The detailed statistical analysis presented here is essential for developing a more quantitative understanding of fission and obtaining better evaluations of fission data for various applications.

First, in Sect. II, we present the framework for the statistical analysis employed for obtaining estimates of the model parameters and the neutron observables, as well as the correlations between the various quantities of interest. We then discuss in Sect. III the experimental

data used in this work with a particular emphasis on experimental uncertainties. Subsequently, in Sect. IV, we describe the physics ingredients of the FREYA simulations. Finally, in Sect. V we present calculated results for the $^{239}\mathrm{Pu}(n,f)$ neutron spectrum and other observables for incident neutron energies, E_n, from 0.5 to 5.5 MeV.

II. STATISTICAL METHOD

Here we briefly describe the statistical method used for determining model parameters and reaction observables.

There are a number of different techniques for estimating model parameter values and although their relative merits are being vigorously debated they often differ very little in their actual results. Our present analysis is inspired by the general inverse problem theory developed by Tarantola [30].

We introduce a number of model parameters $\{\alpha_k\}$ (defined in Sect. IV). Since the theory does not, a priori, specify the parameter values, we assume that the parameter values are uniformly distributed over a reasonable interval in parameter space. For a specified set of parameter values $\{\alpha_k^{(m)}\}$, we generate a large sample of fission events from which we then extract the particular observables of interest, $\{\mathcal{C}_i\}$. These calculated values are then compared with the corresponding experimental values, $\{\mathcal{E}_i\}$.

Specifically, for each parameter set $\{\alpha_k^{(m)}\}$ we calculate the χ^2 deviation of the calculated observables from their measured values,

$$\chi_m^2 \ \equiv \ \chi^2\{\alpha_k^{(m)}\} \ \equiv \ \sum_i \frac{(\mathcal{C}_i\{\alpha_k^{(m)}\} - \mathcal{E}_i)^2}{\sigma_i^2} \ . \qquad (1)$$

Here $\{\sigma_i\}$ are the uncertainties in the experimental values Division by these quantities ensures that well-measured observables carry more weight than those that are poorly measured.

The key feature of the method [30] is that a likelihood is assigned to each particular set m of model parameter values based on how well the corresponding model calculation reproduces the experimental results,

$$w_m \ \equiv \ w\{\alpha_k^{(m)}\} \ \propto \ e^{-\frac{1}{2}\chi^2\{\alpha_k^{(m)}\}} \ . \qquad (2)$$

This quantity is then taken as the relative probability that those parameter values are the "correct" ones. In this manner, one may define a probability density in the space of model parameters, $P\{\alpha_k\} \equiv w\{\alpha_k\}/W$, where $W \equiv \sum_m w_m$ is the sum of all the weights.

Once the probability density of model parameter values has been obtained, their corresponding statistical distribution of the observables can readily be calculated. Thus the *best estimate* for the model parameter values, $\{\tilde{\alpha}_k\}$, is given by the likelihood-weighted average,

$$\tilde{\alpha}_k \ \equiv \ \prec \alpha_k \succ \ \equiv \ \frac{1}{W} \sum_m w_m \alpha_k^{(m)} \ \approx \ \alpha_k^0 \ . \qquad (3)$$

The last relation indicates that the best estimate is approximately equal to the *most likely* value α_k^0, *i.e.* the value having the largest likelihood. The covariances among the parameter values are similiarily calculated,

$$\tilde{\sigma}_{kk'} \ \equiv \ \prec (\alpha_k - \tilde{\alpha}_k)(\alpha_{k'} - \tilde{\alpha}_{k'}) \succ \ . \qquad (4)$$

The diagonal elements, $\tilde{\sigma}_{kk} = \tilde{\sigma}_k^2$, are the usual variances with $\tilde{\sigma}_k$ the standard deviations of the parameter values and represent the squares of the uncertainties on the values of the individual model parameter α_k. The off-diagonal elements give the covariances between two model parameters. It is often more instructive to employ the associated *correlation coefficients*, $C_{kk'} \equiv \tilde{\sigma}_{kk'}/[\tilde{\sigma}_k \tilde{\sigma}_{k'}]$.

An analogous procedure can be carried out to obtain best estimates for the various calculated quantities, *i.e.* for the observables $\{\mathcal{C}_i\}$. Thus, if $\mathcal{C}_i^{(m)} \equiv \mathcal{C}_i\{\alpha_k^{(m)}\}$ denotes the value of $\mathcal{C}_i$ calculated with the particular parameter values $\{\alpha_k^{(m)}\}$, then the best estimate for the observable $\mathcal{C}_i$ is given by

$$\tilde{\mathcal{C}}_i \ \equiv \ \prec \mathcal{C}_i \succ \ = \ \frac{1}{W} \sum_m w_m \mathcal{C}_i^{(m)} \ \approx \ \mathcal{C}_i\{\alpha_k^0\} \ . \qquad (5)$$

The last relation expresses the fact that the best estimate is approximately equal to the most likely result, *i.e.* the result obtained with the most likely parameter values.

Covariances between different observables, $\{\mathcal{C}_i\}$, are calculated as

$$\tilde{\sigma}_{ij} \ \equiv \ \prec (\mathcal{C}_i - \tilde{\mathcal{C}}_i)(\mathcal{C}_j - \tilde{\mathcal{C}}_j) \succ \qquad (6)$$

The diagonal elements are the squares of the standard deviations, $\{\tilde{\sigma}_i\}$, of the calculated values $\{\mathcal{C}_i\}$ resulting from uncertainties in the model parameter values. Here $C_{ij} \equiv \tilde{\sigma}_{ij}/[\tilde{\sigma}_i \tilde{\sigma}_j]$ are the correlation coefficients between the observables $\mathcal{C}_i$ and $\mathcal{C}_j$.
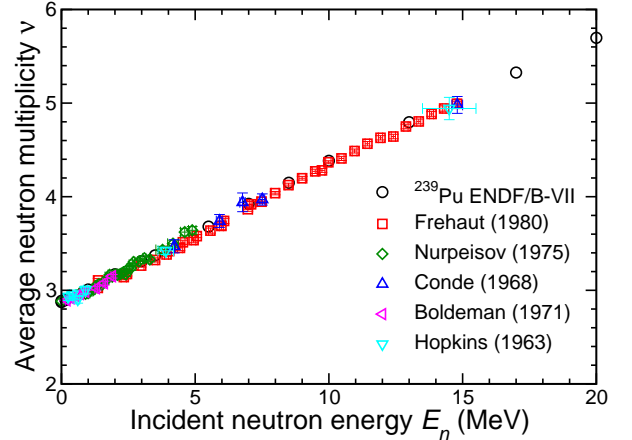

FIG. 1: (Color online.) The evaluated ENDF/B-VII data for the average prompt neutron multiplicity $\overline{\nu}$ as a function of the incoming neutron energy E_n, together with the experimental data from Refs. [10–14].

Data Set	N	$E_{\min}$ (MeV)	$E_{\max}$ (MeV)	a (MeV)	b (MeV)	χ^2/N
Abramson [21]	95	0.55	14.253	1.042	0.5294	2.073
Aleksandrova [20]	54	1.503	11.128	0.914	0.5033	13.474
Aleksandrova [20]	19	1.5	11	0.917	0.5033	14.666
Belov [18]	18	0.3	7	0.991	0.5033	0.868
Conde [17]	13	0.3	7.5	0.975	0.5365	1.121
Knitter [19]	183	0.28	13.87	1.030	0.5040	1.529
Nefedov [22]	65	0.139	7.15	1.023	0.5053	0.765
Starostov [25]	65	3.007	11.2	0.995	0.5288	3.890
Werle [24]	79	0.104	9.5	1.035	0.5263	4.244
Staples (0.5 MeV) [23]	68	0.615	16	1.026	0.5005	4.067
Staples (1.5 MeV) [23]	59	1.7	15.2	1.009	0.5025	8.137
Staples (2.5 MeV) [23]	51	2.77	14.4	1.0276	0.5025	4.018
Staples (3.5 MeV) [23]	38	4.07	13.8	1.0354	0.5025	8.033

TABLE I: For each data set is listed the number of points N, the minimum and maximum measured outgoing neutron energies, the fitted Watt parameters a and b, and the associated χ^2 per degree of freedom.

In principle, the best estimate for the observables $\{\mathcal{C}_i\}$ is neither that resulting from using the most likely parameter values $\{\alpha_k^0\}$ nor that calculated with the best estimate of the model parameters, $\{\tilde{\alpha}_k\}$. In our applications the distinction between the different estimates is mostly one of principle since the different estimates yield practically identical results. We shall generally adopt the observable values calculated with the optimal parameter values, $\{\alpha_k^0\}$, as our estimate while the associated uncertainties and correlations will be obtained on the basis of the entire ensemble, as expressed in Eq. (6).

III. EXPERIMENTAL DATA

We discuss here the experimental data used in our study.

B. Prompt neutron spectrum

Our statistical analysis will also incorporate the measured prompt neutron spectrum [17–23] as given in the EXFOR/CSISRS database. Wherever the experimental uncertainties are not given we have used an uncertainty of 5% in the calculation of χ^2. This is likely an underestimate of the real uncertainty. The various data sets are shown in Fig. 2. The bulk of the data are obtained for low incident neutron energies, $E_n \lesssim 0.5\,\text{MeV}$. The remaining data have been taken by Staples et al. [23] at $E_n = 0.5, 1.5, 2.5,$ and 3.5 MeV.

The data in the top panel of Fig. 2 were taken for incident energies below 0.5 MeV and are not absolutely normalized. In order to compare the data sets with each

A. Mean neutron multiplicity

The mean number of prompt neutrons emitted following neutron-induced fission of ^{239}Pu has been measured in a number of experiments [10–14] and was reviewed by Fort et al. [15]. Figure 1 shows a selection of this data as well as the associated ENDF/B-VII evaluation [16]. We employ the ENDF evaluation as an approximate average of the experimental numbers and we assign a 0.5% uncertainty to $\overline{\nu}$.

other and with our calculated spectra, we normalize all data sets to unity (while preserving the spectral shapes). For this purpose, we fit the observed energy spectra to a Watt spectrum,

$$\frac{dN}{dE} = N_0\, e^{-E/a} \sinh\sqrt{2E/b} , \qquad (7)$$

where the normalization N_0 is determined by demanding that the integral over E yield unity. Table I lists for each data set the number of data points, the minimum and maximum neutron energies observed, the Watt parameters a and b obtained by the fitting procedure, and the associated minimum χ^2 per degree of freedom. The value of a is ≈ 1 MeV within the uncertainties of the fits for all but the Aleksandrova sets where $a \approx 0.91$ MeV. The

value of b is 0.50-0.56 MeV in all cases.

The data on the neutron spectra cover a wide energy range, $0.1 < E < 14$ MeV. In the lowest E range, $E \lesssim 0.5$ MeV, the neutron yields generally increase with E, reaching a maximum somewhere between 0.5 and 1 MeV, and decreasing again above 1 MeV. There is significant disagreement between the data sets in this energy region. In particular, the data of Belov *et al.* [18], Werle *et al.* [24], and Abramson *et al.* [21] have relatively large uncertainties and include points noticeably higher than the remaining data. Curiously, the peak of the $E_n = 0.5$ MeV spectrum from Staples *et al.* [23] is significantly narrower than those of the other data sets. At higher outgoing energies, $E \gtrsim 2$ MeV, all the data sets closely follow each other, except for those from Aleksandrova *et al.* [20] which are systematically lower. Indeed, the Aleksandrova sets are rather poorly represented by the Watt fits, having the largest χ^2 per degree of freedom, see Table I.

Some of the discrepancies between the data sets may be due to the incompleteness of the individual sets in parts of the energy range. For example, the Aleksandrova [20]
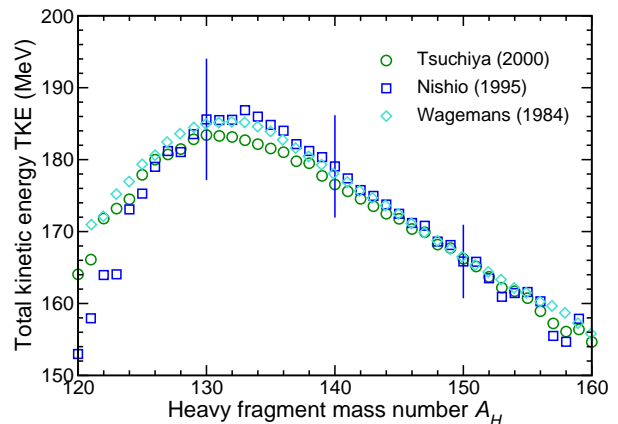
FIG. 3: (Color online.) The average TKE as a function of the heavy fragment mass A_H, from Refs. [26–28].

and Starostov [25] sets are only available for E above 1.5 and 3 MeV, respectively, so that the Watt fits may match the high energy tail of the spectrum but cannot represent the peak region and below. Similarly, sets that cover the region $E < 7$ MeV may not give as good fits to the high-energy part of the spectrum. When $E_n \geq 1.5$ MeV, the minimum outgoing energy E measured by Staples *et al.* [23] (shown in the lower panel of Fig. 2) is always greater than E_n. Thus these data sets do not provide much information on the softer part of the spectrum and the back extrapolation by means of the Watt form is somewhat unreliable since the measured hard spectra do in fact not fit a Watt shape very well, as reflected by the large values of χ^2 in Table I.

C. Fission fragment energies

Several measurements of the total kinetic energy (TKE) of the two fission fragments can be found in the literature. Figure 3 shows the principal measurements of the mean TKE as a function of the mass number of the heavy fragment, A_H, which were made by Wagemans *et al.* [26], Nishio *et al.* [27], and Tsuchiya *et al.* [28]. (The mass number of the heavy fragment is found by simultaneously measuring the velocities and energies of both fragments [27]. No experimental uncertainties are given for these results, neither for the mass number nor for the reported TKE.) The data exhibit a significant dip near symmetry and fall off steadily for large asymmetries, resulting in a maximum at $A_H \approx 133$. The different data sets generally agree well for large A_H but they exhibit a significant spread near symmetry. Furthermore, Ref. [27] also provides the full-width at half-maximum (FWHM) of the TKE distribution at selected values of A_H. These also decrease at large A_H, reflecting the fact that the TKE spectrum softens, presumably because the mutual Coulomb repulsion between the two nascent fragments decreases with larger asymmetry.
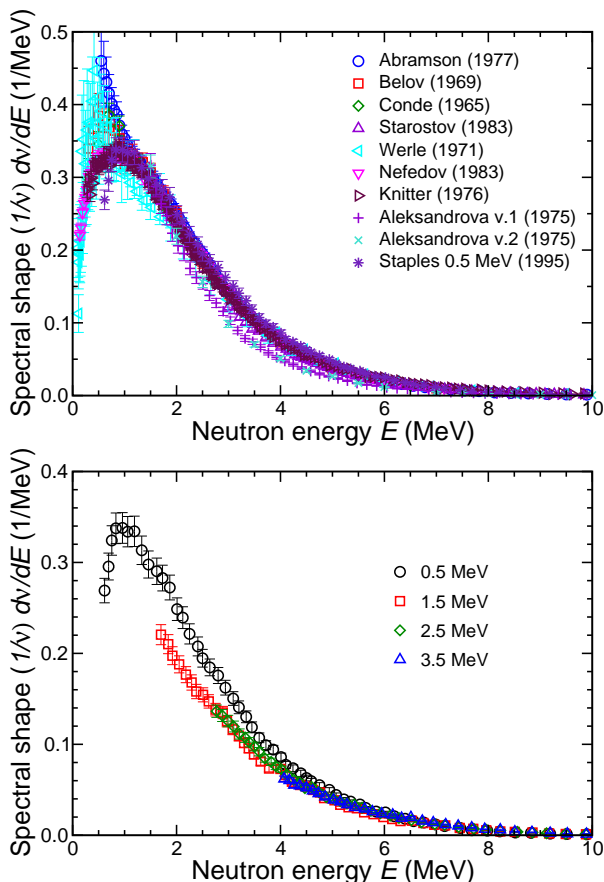

FIG. 2: (Color online.) The measured prompt neutron energy spectra, normalized to unity, as a function of outgoing neutron energy for low incident energies from Refs. [17–25] (*upper panel*) and for a wider range of incident energies from Ref. [23] (*lower panel*).

IV. GENERATION OF FISSION EVENTS

We have adapted the recently developed fission model FREYA [29] for the present purpose of calculating the neutron spectrum in terms of a set of well-defined model parameters. Since this is the first practical application of FREYA, we describe its main physics ingredients below.

The code follows the temporal sequence of individual fission events from the initial excited fissionable nucleus, ^{240}Pu* in the present case, through a scission configuration of the two nascent fragments, to the subsequent neutron evaporation from the fully accelerated fragments. The competition between fission and neutron emission from the fissioning nucleus (2$^{\rm nd}$ chance fission) has not yet been implemented in the code. Consequently, we restrict our discussion to energies below 5.5 MeV.

A. Fission mass and charge partition

The fission process is initiated when a neutron with a specified initial energy E_n is absorbed by a fissile nucleus to form a compound nucleus $^A Z$ with a certain excitation energy. The compound nucleus subsequently splits into a heavy fragment $^{A_H} Z_H$ and a complementary light fragment $^{A_L} Z_L$. In its present early form, FREYA selects the mass and charge partitions on the basis of existing experimental data. For the present study, we use fits to the thermal and fast ^{239}Pu(n,f) fission product mass yields measured by England and Rider [31] in combination with the charge distributions obtained by Reisdorf et al. [32].

The fits assume that the mass product yields $Y(A_p)$ exhibit three distinct fission modes that can be represented in terms of suitable gaussians,

$$Y(A_p) = S_1(A_p) + S_2(A_p) + S_L(A_p) . \quad (8)$$

The first two terms result from asymmetric fission modes associated with the spherical shell closure at $N = 82$ and the deformed shell closure at $N = 88$ respectively, while the last term results from a symmetric, so-called superlong, mode which is relatively insignificant [33]. The specific forms of these terms are

$$S_i = \frac{N_i}{\sqrt{2\pi}\sigma_i} \left[e^{-(A-\bar A-D_i)^2/2\sigma_i^2} + e^{-(A-\bar A+D_i)^2/2\sigma_i^2} \right] \quad (9)$$

for $i = 1, 2$ and

$$S_L = \frac{N_L}{\sqrt{2\pi}\sigma_L} e^{-(A-\bar A)^2/2\sigma_L^2} . \quad (10)$$

Here $\bar A = \frac{1}{2}(A_0 - \bar\nu)$, where $A_0 = 240$ is the mass number of the fissioning nucleus and $\bar\nu$ is the average total multiplicity of evaporated neutrons. (While there exist more detailed data for e.g. ^{235}U(n,f) that give the yields as a function of both mass and total kinetic energy, $Y(A_p, {\rm TKE})$, for several values of E_n [34], such data are not yet available for Pu.)

The values of the parameters in the fits to $Y(A_p)$ are given in Table II for either thermal or fast fission. The normalization is chosen such that $\sum_A Y(A) = 2$ since each event leads to two products. Consequently we have $2N_1 + 2N_2 + N_L = 2$, apart from a negligible correction because A_p is discrete quantity bounded both from below and above. It should be noted that the symmetric component contributes only 1-2 per mille of the yield.

While these fits are to the fission product yields, the FREYA simulation requires fission fragment yields, i.e. the probability distribution for obtaining a given mass partition at scission, before neutron evaporation has begun, We take $\bar A \approx \frac{1}{2}A_0$, but keep the displacements D_i and the widths σ_i unchanged. We use the thermal fits for $E_n < 1$ MeV and the fast fits for $1 < E_n < 5.5$ MeV, the highest value of E_n considered here. The change in the fit parameter values with incident neutron energy should, of course, be more continuous than we have implemented here but the change is most important in areas where the yields are low: the tails of the gaussians where fission is most asymmetric and in the case of symmetric fission. At even higher energies, symmetric fission (the S_L component) grows increasingly important, filling in the dip at symmetry. The width σ_2 also increases, broadening the asymmetric tails.

The resulting fits are compared to the data in Figs. 4 and 5. The agreement with the tabulated percentage yields is quite good, especially in the regions where the yields are highest and which thus contribute the greatest number of events. Equation (8) does not perfectly describe the tails at high and low fragment mass. We have also tried a fit with 5 independent gaussians, e.g. allowing N_i, D_i and σ_i to vary independently on the low and high sides of $\overline A$, and found that the fit does not significantly improve as a result. We note also that the width of the S_L component is not as large as found in other actinides where the yields have been decomposed in a similar fashion [34].

Once the gaussian fit has been fixed, it is straightforward to make a statistical selection of the fragment mass number A_f. The mass number of the partner fragment is then readily determined since we assume $A_L + A_H = A_0$.

Parameter	Thermal	Fast
$\bar A$	118.5	117.5
N_1	0.7574	0.7355
D_1	20.81	20.96
σ_1	5.626	5.711
N_2	0.2417	0.2623
D_2	14.95	15.14
σ_2	2.546	2.627
N_L	0.0018	0.0044
σ_L	1.824	2.511

TABLE II: The fit parameters of the three fission modes for thermal and fast neutron-induced fission on ^{239}Pu.
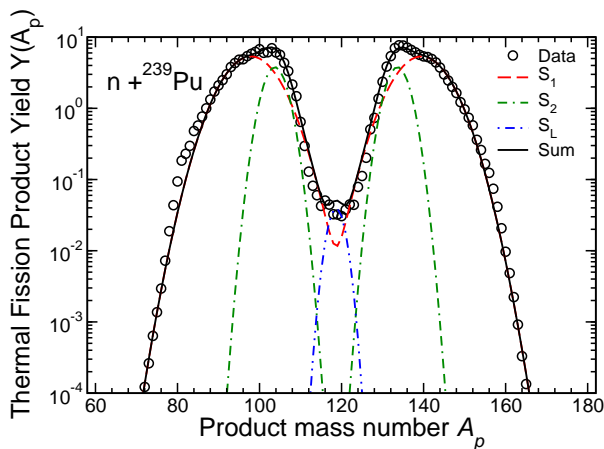
FIG. 4: (Color online.) The fission product yield as a function of fragment mass for thermal fission. The data are from Ref. [31] while the curves are a five-gaussian fit to the data.
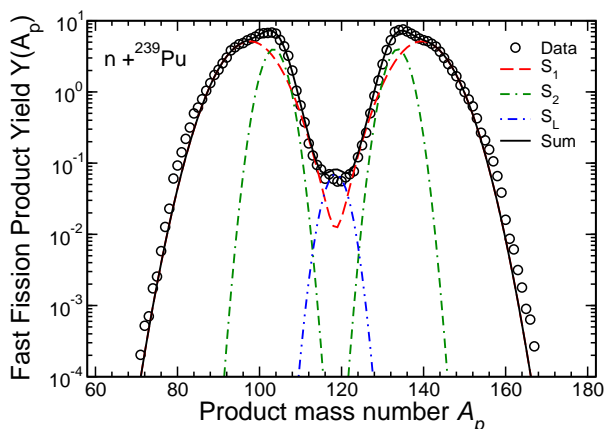

FIG. 5: (Color online.) Same as Fig. 4, but for fast-neutron induced fission.

The fragment charge, Z_f, is selected subsequently. For this we follow Ref. [32] and employ a gaussian form,

$$P_{A_f}(Z_f) \propto e^{-(Z_f - \bar{Z}_f(A_f))^2/2\sigma_Z^2} , \qquad (11)$$

with the condition that $|Z_f - \bar{Z}_f(A_f)| \leq 5\sigma_Z$. The centroid is determined by requiring that the fragments have, on average, the same charge-to-mass ratio as the fissioning nucleus, $\bar{Z}_f(A_f) = A_f Z_0/A_0$. The dispersion is the measured value, $\sigma_Z = 0.5$ [32]. The charge of the complementary fragment then follows using $Z_L + Z_H = Z_0$.

B. Fragment energies

Once the partition of the total mass and charge among the two fragments has been determined, the Q value associated with that particular channel follows as the difference between the mass of the excited compound nucleus,

^{240}Pu*, and ground-state masses of the two fragments,

$$Q_{LH} = M(^{240}\text{Pu}^*) - M_L - M_H . \qquad (12)$$

FREYA takes the required nuclear ground-state masses from the compilation by Audi *et al.* [35], supplemented by the calculated masses of Möller *et al.* [36] where no data are available. The Q_{LH} value for the selected fission channel is then divided up between the total kinetic energy (TKE) and the total excitation energy (TXE) of the two fragments. The specific procedure employed is described below.

First, the average value of TKE is determined on the basis of the Coulomb potential between the two fragments at scission,

$$\overline{\text{TKE}} = e^2 \frac{Z_L Z_H}{c_L + c_H + d_{LH}} . \qquad (13)$$

In the scission configuration, the two nascent fragments are assumed to have spheroidal shapes and be positioned coaxially with a tip separation of d_{LH}. The associated major axes are $c_i = r_0 A_i^{1/3}/[1 - \frac{2}{3}\varepsilon(Z_i, A_i)]$ with $r_0 = 1.2$ fm. We use the values for the spheroidal deformation parameter $\varepsilon(Z_i, A_i)$ calculated in Ref. [36] which include shell effects. The denominator of Eq. (13) is thus the distance between the centers of the two fragments and the above expression represents the monopole-monopole term of the mutual Coulomb interaction energy.

The tip separations $\{d_{LH}\}$ are important parameters in the model since they determine the (average) fragment kinetic energies and hence, by energy conservation, also the total fragment excitation that is available for neutron emission. Thus the neutron emission is quite sensitive to the specified values of $\{d_{LH}\}$ and they deserve careful consideration. Furthermore, since the TKE is closely related to the Coulomb potential at scission, these parameters contain valuable information about the scission configurations.

Figure 6 shows the mean total fragment kinetic energy as a function of mass number of the heavy fragment as obtained by using a common tip separation d_0 for all fission channels. A comparison to the data [26–28] shows significant discrepancies near symmetry where the calculated TKE exhibit an enhancement whereas the data have a dip.

To account for the dependence of the tip separation on the mass partition, we took the average of the data sets shown in Fig. 6 and extracted the average tip separations $\underline{d}_{LH}$ shown in Fig. 7, assuming that the two fragments have the same charge-to-mass ratio. Near symmetric fission, $\underline{d}_{LH}$ is large, 7-8 fm at $A_H = 120$, with a steep drop to less than 4 fm for $A_H \geq 132$. Near symmetry, the plutonium fission fragments are mid-shell nuclei subject to strong deformation. Thus the scission configuration will contain significant deformation energy and a correspondingly large distance between centers, resulting in low TKE. At $A_H = 132$, the heavy fragment is close to the doubly-magic closed shell with $Z_H = 50$, $N_H = 82$
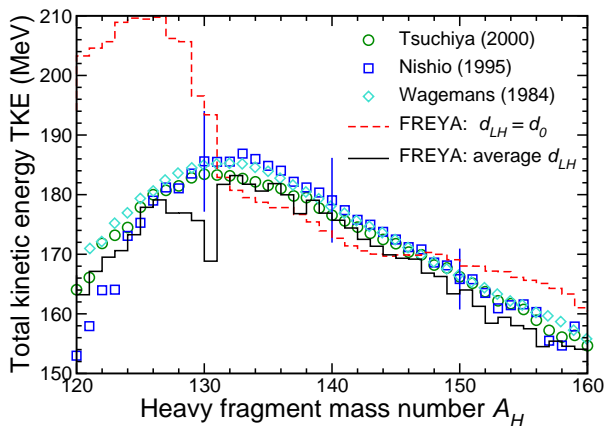
FIG. 6: (Color online.) The measured average TKE as a function of the mass number of the heavy fragment [26–28] compared to FREYA calculations with a constant tip separation of d_0=4.05 fm and the average distance extracted from Fig. 7.
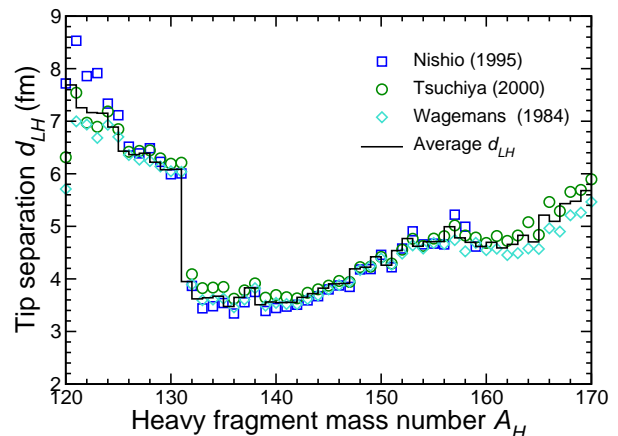

FIG. 7: (Color online.) The tip separation d_{LH} fitted to the TKE values measured at thermal energies [26–28], with the deformation radii extracted from the mass model of Ref. [36].
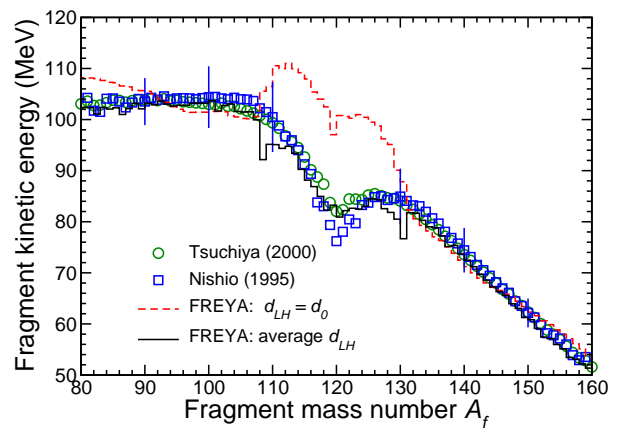

FIG. 8: (Color online.) The average fragment kinetic energy as a function of fragment mass from Refs. [27, 28] compared to FREYA calculations with a constant tip separation of $d_0 = 4.05$ fm and the average distance extracted from Fig. 7.

and is resistant to distortions away from its spherical shape. However, the complementary light fragment is far from a closed shell and is significantly deformed, having thus a large value of c_L which then results in a small tip separation $\underline{d}_{LH}$ and a large TKE. The passage of the heavy fragment mass through the doubly-magic region results in the dip in calculated TKE around $A_H \sim 130$, see Fig. 6.

The TKE values shown in Fig. 6 were obtained in experiments with incident neutrons of very low energy and there are no other higher-energy data to show how $\text{TKE}(A_H)$ evolves with incident neutron energy. At each higher incident energy $E_n > E_{\text{thermal}}$, we use tip separations obtained by scaling those fitted at thermal energies,

$$d_{LH}(E_n) = s(E_n)d_{LH}(E_{\text{thermal}}) , \qquad (14)$$

and use the common scaling factor $s(E_n)$ as one of the adjustable model parameters in our fits to the neutron spectra. The average neutron multiplicity is very sensitive to this scale factor which, as we shall show, is greater than but very close to unity for the entire energy range studied.

As shown in Fig. 6, the scaled tip separations lead to a very good agreement with the TKE data. With this means of fixing d_{LH}, the TKE is no longer overestimated near symmetry, leading to a better approximation of the individual fragment kinetic energy as well as the neutron multiplicity as a function of fragment mass, overestimated and underestimated respectively with a constant value of d_{LH}, as shown in Figs. 8 and 9. The variable d_{LH} also correctly produces the dip in the single fragment kinetic energy shown in Fig. 8. The small dips in the fragment kinetic energy at $A = 110$ and 130 correspond to the dip at $A_H \sim 130$ in Fig. 6.

The overestimate of the total fragment kinetic energy with a constant d_{LH} leaves insufficient excitation energy available for neutron evaporation near symmetry, resulting in the near absence of neutron emission in Fig. 9 in

this case. On the other hand, with d_{LH} from Fig. 7, there is a peak in the neutron emission near symmetry, followed by a drop for $A > 120$, resulting in the characteristic sawtooth shape of $\nu(A)$. The decrease in KE for these values of A gives small peaks in the neutron multiplicity at the same values of A. Interestingly enough, the calculations with both fixed and variable d_{LH}, give the same $\overline{\nu}$ even though $\overline{\nu}(A_f)$ is very different in the two cases. It is easy to see why this is true by looking at Figs. 4 and 9 together. Symmetric fission does not contribute significantly to the total yield, $Y(A_f)$. Most of the fragment yield is around $A_L \sim 100$, $A_H \sim 140$. The variable d_{LH} gives more neutrons for symmetric fission and in regions of high A_H (low A_L) with lower yields and fewer neutrons where $Y(A_f)$ is large to obtain the same $\overline{\nu}$ as the constant d_{LH} where the neutrons from symmetric fission are effectively absent.

Once the average total fragment kinetic energy has been determined, the average combined excitation en-
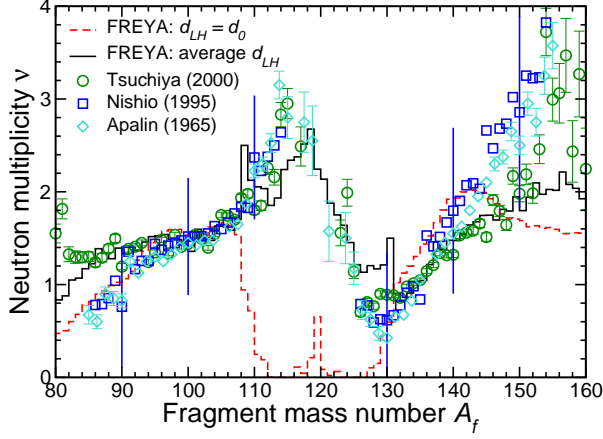
FIG. 9: (Color online.) The average neutron multiplicity as a function of the fragment mass from Refs. [27, 28, 37] compared to FREYA calculations with a constant tip separation of $d_0 = 4.05$ fm and the average distance extracted from Fig. 7.

ergy in the two fragments follows automatically by energy conservation,

$$Q_{LH} - \overline{\text{TKE}} = \overline{\text{TXE}} = \overline{E}_L^* + \overline{E}_H^* . \tag{15}$$

The last relation indicates that the total excitation energy is partitioned between the two fragments. The variation of the total mean excitation energy with fragment mass is similar to that of $\overline{\nu}(A)$ in Fig. 9.

FREYA assumes that the excitation energy is partitioned statistically, as it would be if the two fragments were in mutual thermal equilibrium. Consequently, $\overline{\text{TXE}}$ is divided in proportion to the heat capacities of the nascent fragments,

$$\overline{E}_i^* = \frac{\tilde{a}_i}{\tilde{a}_L + \tilde{a}_H} \overline{\text{TXE}} , \tag{16}$$

where $\tilde{a}_i$ is the level-density parameter for fragment i. To take account of the microscopic structure of the individual fragments as well as any possible energy dependence, FREYA uses the functional form due to Kawano *et al.* [38],

$$\tilde{a}_i(E_i^*) = \frac{A_i}{e_0} \left[1 + \frac{\delta W_i}{U_i} [1 - e^{-\gamma U_i}] \right] \tag{17}$$

where $U_i = E_i^* - \Delta_i$ and $\gamma = 0.05$ [9]. The pairing energy of the fragment, Δ_i, and its shell correction, δW_i are tabulated in Ref. [38] based on the mass formula of Koura *et al.* [39]. Although FREYA uses the default value $e_0 = 7.25$ MeV [29], we wish to make this value adjustable, taking

$$e_0 = (7.25\,\text{MeV})\,a \tag{18}$$

and treating the common factor a as a model parameter. We note that if the shell corrections are negligible, $\delta W \approx 0$, then this renormalization is immaterial and the excitation energy will be shared according to mass, $\bar{E}_i^* \propto A_i$.

The relationship between excitation energy E_i^* and the temperature T_i is given by

$$E_i^* = \tilde{a}_i T_i^2 \tag{19}$$

so that when the total excitation energy is shared according to the level-density parameters $\tilde{a}_i$ then the two fragment temperatures are equal, $T_L = T_H$.

While the equal temperature assumption is a reasonably good first approximation, it may be inadequate for obtaining a detailed description of prompt neutron emission. Therefore we redistribute the excitation energies of the fragments,

$$\tilde{E}_L^* = x\bar{E}_L^* , \ \tilde{E}_H^* = \overline{\text{TKE}} - \tilde{E}_L^* , \tag{20}$$

and treat x as an adjustable model parameter. The data indicate that the light fragments acquire more than their "fair share" of the energy, thus we expect that our statistical analysis will favor $x > 1$.

After the mean excitation energies have been assigned, FREYA considers the effect of thermal fluctuations in the partitioning of the excitation energy. For this task, FREYA assumes that the fluctuation in the excitation energy of a nucleus is $\sigma_E^2 = 2\bar{E}^*T$ where T is its temperature and $\bar{E}^* = \tilde{a}T^2$ its mean excitation. Therefore, for each of the two fragments, we sample a thermal energy fluctuation δE_i^* from a gaussian distribution of variance $\sigma_i^2 = 2\tilde{E}_i^*T_i$ and modify the fragment excitations accordingly,

$$E_i^* = \tilde{E}_i^* + \delta E_i^* , \ i = L, H . \tag{21}$$

Due to energy conservation, there is a compensating opposite fluctuation in the total kinetic energy, so

$$\text{TKE} = \overline{\text{TKE}} - \delta E_L^* - \delta E_H^* . \tag{22}$$

With both the excitations and the kinetic energies of the two fragments fully determined, it is an elementary matter to calculate the magnitude of their momenta and thus sample the velocities with which they emerge after having been fully accelerated by their mutual Coulomb repulsion [29].

C. Neutron evaporation

The primary fission fragments are typically sufficiently excited to permit the emission of one or more neutrons. For each of the two fragments, neutron emission is treated by iterating neutron evaporation from each fragment.

At each step in the evaporation chain, the excited mother nucleus $^{A_i}Z_i$ has a total mass equal to its ground-state mass plus its excitation energy, $M_i^* = M_i^{\text{gs}} + E_i^*$. The Q-value for neutron emission from the fragment is then $Q_n = M_i^* - M_f - m_n$, where M_f is the ground-state mass of the daughter nucleus and m_n is the mass of the neutron (for neutron emission we have $A_f = A_i - 1$ and $Z_f = Z_i$). The Q-value is equal to the maximum possible excitation energy of the daughter nucleus, which occurs

if the final relative kinetic energy vanishes. The temperature in the daughter fragment is then maximal. Thus, once Q_n is known, one may sample the kinetic energy of the evaporated neutron. FREYA assumes that the angular distribution is isotropic in the rest frame of the mother nucleus and uses a standard spectral shape [40],

$$f_n(E) \equiv \frac{1}{\overline{\nu}} \frac{d\overline{\nu}}{dE} \propto E \, e^{-E/T_f^{\max}} \, , \qquad (23)$$

which can be sampled very fast [29].

Although relativistic effects are very small, we take them into account in order to ensure exact conservation of energy and momentum, which is convenient for code verification purposes. We therefore take the sampled energy E to represent the *total* kinetic energy in the rest frame of the mother nucleus, *i.e.* it is the kinetic energy of the emitted neutron *plus* the recoil energy of the residual daughter nucleus. The excitation energy in the daughter nucleus is then given by

$$E_d^* = Q_n - E \, . \qquad (24)$$

The mass of the daughter nucleus is thus $M_d^* = M_d^{\mathrm{gs}} + E_d^*$. It is possible to calculate the magnitude of the momenta of the two final bodies: the excited daughter and the emitted neutron. Sampling the direction of their relative motion isotropically, we thus obtain the two final momenta which are subsequently boosted into the overall reference frame by the appropriate Lorentz transformation.

This procedure repeated until no further neutron emission is energetically possible, when $E_d^* < S_n$, where S_n is the neutron separation energy for the daughter nucleus, $S_n = M(^{A_d}Z_d) - M(^{A_d-1}Z_d) - m_n$.

V. RESULTS

We now proceed to discuss our analysis. We first describe the computational approach and then explain how the model parameters are determined. The resulting prompt neutron spectrum is then discussed in detail. Finally, we present some additional observables of particular relevance.

A. Computational approach

FREYA is used to generate a large sample of fission events (typically one million events for each parameter set). For each set m of such randomly selected model parameter values, $\{s^{(m)}, a^{(m)}, x^{(m)}\}$, the prompt fission neutron spectrum and $\overline{\nu}$ in each event m are then compared to the available experimental data at the given incident neutron energy, E_n. This allows us to assign the likelihood for that particular set (see Sec. II) based on either the χ_m^2 for comparison with $\overline{\nu}$ only, $\chi_{\overline{\nu}}^2$, or on the total χ_m^2 characterizing the comparison with both $\overline{\nu}$ and the spectral shape $f_n(E) = \overline{\nu}^{-1} d\overline{\nu}/dE$, $\chi_{\overline{\nu}}^2 + \chi_{\mathrm{spectra}}^2$,

$$w_m = w\{s^{(m)}, a^{(m)}, x^{(m)}\} = e^{-\chi_m^2/2} \, . \qquad (25)$$

Since the weight w_m depends exponentially on χ_m^2, the likelihood tends to be strongly peaked around the favored set. It is important that the parameter sample be sufficiently dense in the peak region to ensure that many sets have non-negligible weights. We typically sample 2000 different parameter sets but have verified that the results remain unchanged when a five times larger sample is explored.

Using this method, we can obtain those values of s, a and x that minimize either $\chi_{\overline{\nu}}^2$ or $\chi_{\overline{\nu}}^2 + \chi_{\mathrm{spectra}}^2$. We denote the optimal set by $\{s^0, a^0, x^0\}$. We also obtain the corresponding correlation matrix, as described in Sec. II.

E_n (MeV)	s^0	a^0	x^0	$\overline{\nu}$	$\chi_{\overline{\nu}}^2$	$\chi_{\mathrm{spectra}}^2/N$
0.5	1.05449 ± 0.00567	1.10562 ± 0.07987	1.10264 ± 0.05909	2.948 ± 0.015	4.26×10^{-3}	28.99
1.5	1.05887 ± 0.00585	1.10426 ± 0.07854	1.10178 ± 0.05736	3.090 ± 0.015	8.46×10^{-4}	9.81
2.5	1.06590 ± 0.00858	1.10243 ± 0.07972	1.09969 ± 0.11359	3.242 ± 0.016	1.88×10^{-2}	3.40
3.5	1.06886 ± 0.00902	1.10440 ± 0.07903	1.09987 ± 0.11745	3.373 ± 0.017	3.78×10^{-2}	5.90
4.5	1.07598 ± 0.00699	1.10246 ± 0.07963	1.09889 ± 0.05829	3.527 ± 0.017	2.55×10^{-2}	–
5.5	1.08418 ± 0.00752	1.10409 ± 0.08023	1.09892 ± 0.05758	3.681 ± 0.019	1.50×10^{-2}	–

TABLE III: The optimal values of the three model parameters s, a and x obtained in three-parameter fits to $\overline{\nu}$ alone, as well as the corresponding mean neutron multiplicities $\overline{\nu}$, together with the extracted uncertainties. The resulting values of $\chi_{\overline{\nu}}^2$ and $\chi_{\mathrm{spectra}}^2$ per degree of freedom are also given.

B. Determination of the model parameters

Table III shows the optimal values and the associated uncertainties for the three model parameters used in our

fission calculations. These values have been obtained by

E_n (MeV)	s^0	a^0	x^0	$\overline{\nu}$	$\chi^2_{\overline{\nu}}$	$\chi^2_{\text{spectra}}/N$
0.5	1.05705 ± 0.00173	0.96754 ± 0.02236	1.00523 ± 0.00574	2.961 ± 0.007	0.76	13.72
1.5	1.04573 ± 0.00742	0.97291 ± 0.03424	1.18356 ± 0.05142	3.078 ± 0.020	0.43	23.77
2.5	1.05485 ± 0.00602	0.99909 ± 0.04221	1.18587 ± 0.06274	3.239 ± 0.016	0.0066	2.58
3.5	1.05309 ± 0.00657	0.98038 ± 0.03839	1.21052 ± 0.05293	3.364 ± 0.013	0.24	4.61

TABLE V: The optimal values s^0, a^0 and x^0 obtained in three-parameter fits to the spectra and $\overline{\nu}$. The corresponding values of $\overline{\nu}$ are also shown. The resulting χ^2 values for $\overline{\nu}$ and the spectra are given separately.

fitting only to the evaluated $\overline{\nu}$ while ignoring the spectral data. We have checked that fixing either x or a, or both, in these fits lead to equivalent results for all values of E_n.

The correlation coefficients between these model parameters are shown in Table IV. If the parameters are uncorrelated, $C_{kk'} = 0$. Correlated parameters lead to nonzero correlation coefficients. If $C_{kk'} > 0$, α_k increases as $\alpha_{k'}$ increases. On the other hand, if $C_{kk'} < 0$, α_k increases as $\alpha_{k'}$ decreases. The correlation coefficients between s and a, C_{sa}, are relatively large and positive while those between s and x, C_{sx}, are large and negative, suggesting strong correlations between these pairs of parameters. The correlation coefficients between a and x, C_{ax}, are close to zero and fluctuate in sign, signaling only a weak correlation between this pair of parameters. In contrast, when the spectra are also included in the fits for $E_n \leq 3.5$ MeV, the correlation coefficients are all very close to ± 1 in all cases, likely because the overlap in parameter space that simultaneously reproduces $\overline{\nu}$ and the spectra is small.

E_n (MeV)	C_{sa}	C_{sx}	C_{ax}
0.5	0.608	-0.569	0.0156
1.5	0.611	-0.561	0.0042
2.5	0.465	-0.776	0.0212
3.5	0.464	-0.766	0.0441
4.5	0.757	-0.569	-0.0053
5.5	0.693	-0.480	-0.0130

TABLE IV: The correlation coefficients (see Eq. (4)) for the three parameters s, a and x fitted to $\overline{\nu}$ alone.

The experimental values for the total average neutron multiplicity place remarkably stringent constraints on the value of the model parameter s while more room is left for variations of a and x. Specifically, changing the tip separation distance scale factor s by only 1% (keeping a and x fixed) changes $\overline{\nu}$ by 1.8%, far outside the experimental uncertainty. A change in s, see Eq. (14), results

in a change in the average TKE, Eq. (13), of less than 0.5 MeV. Thus $\overline{\nu}$ is very sensitive to the balance between the kinetic and excitation energies. On the other hand, $\overline{\nu}$ is less sensitive to the partition of the excitation energy between the light and heavy fragments since changing x by 5% (keeping a and s fixed) changes $\overline{\nu}$ by only 0.5%. Finally, $\overline{\nu}$ is least sensitive to changes in a which modifies the fragment temperature, predominantly affecting the low energy part of the neutron spectrum. Changing a by 5% (keeping s and x fixed) changes $\overline{\nu}$ by only 0.3%.

Table V shows results calculated by fitting to both $\overline{\nu}$ and the prompt neutron spectra. (We do not show the 4.5 and 5.5 MeV results again since there are no published spectra at these energies.) When the spectral data are included in the fit the agreement with these data and the evaluated $\overline{\nu}$ is poor. If we had confidence in the spectral data, this would be a formal indication that our model was incorrect or that uncertainties in $\overline{\nu}$ were underestimated. Inconsistencies in the spectral data (see Sect. III B) make either conclusion difficult. Some sets (particularly those of Alexandrova [20], which make the largest contribution to the spectral χ^2) are inconsistent with other sets, and, in a number of cases, uncertainties conservatively estimated. In addition, the relative normalization, while determined from fitting to a Watt spectrum and used only for scaling purposes, may increase the relative χ^2 for some data sets, possibly including the Aleksandrova sets which are only available for $E > 1.5$ MeV. Indeed, since these sets give the largest contribution to the total χ^2, eliminating them can change the optimal parameter values, while removing one or more of the other sets has little to no effect. For these reasons, we did not use the spectral data to obtain our final evaluation. In addition, as discussed in more detail later, there are indications from ^{235}U measurements that more neutrons are emitted from the light fragment than are from the heavy fragment ($x > 1$) [27]. The fit at E_n=0.5 MeV shown in Table V is consistent with $x = 1$, giving $\overline{\nu}_L \approx \overline{\nu}_H$.

C. The prompt neutron spectrum

A comparison between experimental data and our calculations of the prompt neutron spectrum is shown in

Fig. 10. The top panel of this figure gives the spectral shape and shows all experimental data from Refs. [17–

25]. Since the shape varies slowly with incident neutron energy, the calculations using parameters fit to $\overline{\nu}$ alone and to $\overline{\nu}$ and the spectral data are practically indistinguishable on a linear scale. The bottom panel of Fig. 10 shows only the more recent Staples data from 0.5 to 3.5 MeV [23]. In this panel, the different spectra can be distinguished because they have been normalized to $\overline{\nu}$, which varies modestly with incident neutron energy.

Because FREYA cannot produce sufficient statistics at the fine energy scale needed by typical spectral evaluations, high statistics FREYA runs have been made to emphasize the low and high energy tails of the spectra. To remove statistical noise, Watt distributions are fit to the low ($E < 2$ MeV) and high ($E > 4$ MeV) energy parts of the spectrum for each incident neutron energy. A fine grid is obtained in the intermediate part of the spectrum by interpolation.

Figure 11 gives the difference between the present calculations and the evaluations in ENDF/B-VII. Our spectra are systematically softer, giving lower mean neutron energies. This difference has important implications for criticality.

In the previous section, we argued that currrently available spectral data should not be used in the fission likelihood analysis. To illustrate the impact of these data on spectral calculations, we show the difference between the fits without and with the spectral data at $E_n = 0.5$ MeV, normalized to $\overline{\nu}$ on a log-log scale, in Fig. 12. The difference is largest in the high-energy tail of the spectra where the fit to the spectra and $\overline{\nu}$ is softer. The ratio of the fits with and without the spectral data are shown in Fig. 13. Below 2 MeV, the fit with the spectral data is 1-2% higher but by $E \approx 10$ MeV, it is about 60% lower than the spectral description with a fit to $\overline{\nu}$ alone. At higher energies the calculations grow further apart but the ratios are statistics limited since, even with 1-2 million events FREYA does not fully populate the high energy tail of the emission spectrum.

We can compute the uncertainty in the spectra as well as in the employed values of the model parameters. Each particular set of model parameter values, $\{\alpha_k^{(m)}\}$, yields a different neutron spectrum $(d\nu/dE)^{(m)}$ so that the resulting ensemble of spectra can be subjected a statistical analysis at each value of the neutron energy E, yielding an average value of the neutron spectrum, $d\tilde{\nu}/dE$, and an associated dispersion, $\sigma(d\nu/dE)$. For $E_n = 0.5$ MeV, Fig. 14 shows the ratio between $d\tilde{\nu}/dE + \sigma(d\nu/dE)$ and $d\tilde{\nu}/dE$. This spectral ratio provides an indication of the relative uncertainty on the spectrum at each energy. With the fits to $\overline{\nu}$ alone, the calculated uncertainty is less than 5% for $E < 4$ MeV and less than 2% for $E < 2$ MeV, much smaller than the spread in the data depicted in Fig. 10. The uncertainty increases approximately linearly with E for $E > 2.5$ MeV, reaching $\approx 40\%$ at 15 MeV. We have also shown the relative uncertainty with all spectra included in the fit as well as that obtained by leaving out the two spectra with the largest χ^2. Both of these give small but noisy uncertainties, suggesting that
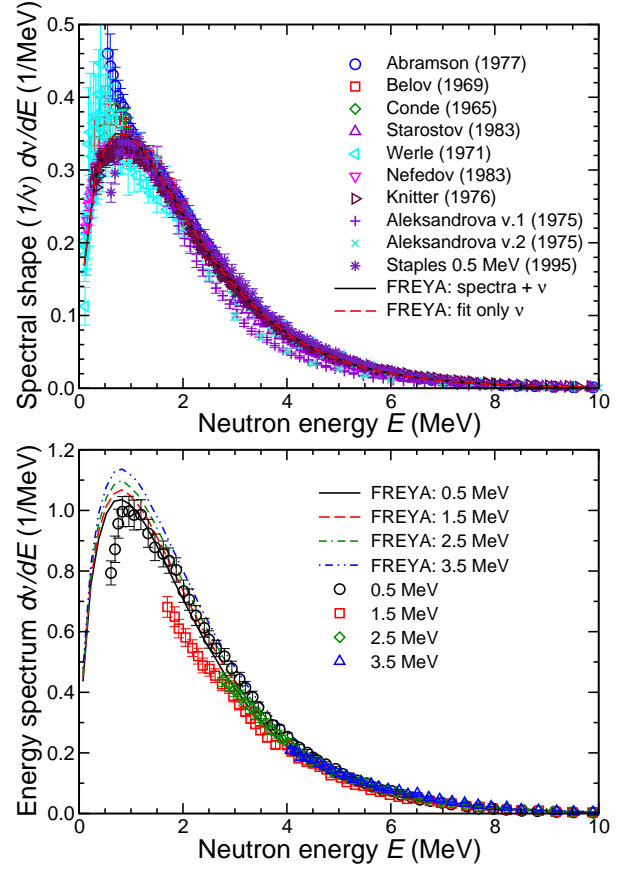

FIG. 10: (Color online.) The measured prompt neutron spectra are compared to our fit results. The comparison to the low energy results from Refs. [17–25] (*upper panel*) are of the normalized spectral shapes while the results at higher incident neutron energies from Ref. [23] (*lower panel*) are compared to the spectral distributions themselves.

result is not a true measure of the calculated uncertainty in this case and that the spectral uncertainty as shown is rather random. The noisiness of the combined fits is due to the difficulty of obtaining a combination of parameter values that simultaneously minimizes χ_ν^2 and χ_{spectra}^2.

It is instructive to consider the correlations between the spectral strength at different energies. The evaluation of the corresponding covariance (see Eq. (6)) is complicated by the fact that the observables considered, specified energies of emitted neutrons, form a continuum. In practice, it is convenient to consider discrete energy bins (so the observable α_k represents the mean number of neutrons emitted with a kinetic energy in the bin k centered at the energy value E_k. Using Eq. (4), we may then calculate the corresponding covariance matrix

$$\tilde{\sigma}(E_k, E_{k'}) = \prec (E_k - \tilde{E}_k)(E_{k'} - \tilde{E}_{k'}) \succ . \quad (26)$$

However, it is important to recognize that for continuous observables, the above matrix function is singular

along the diagonal [42],

$$\tilde{\sigma}(E_k, E_{k'}) \; = \; \tilde{\sigma}_{E_k}^2 \, \delta(E_k - E_{k'}) + \tilde{\sigma}_{E_k E_{k'}} \; , \qquad (27)$$

where $\tilde{\sigma}_{E_k}^2$ is the variance in the differential yield at the specified energy E_k, while $\tilde{\sigma}_{E_k E_{k'}}$ expresses the correlation between the differential yields at two *different* energies E_k and $E_{k'}$. To obtain this latter quantity, we must first remove the singular part. This can be readily accomplished when the observable has been discretized by simply replacing the diagonal elements in $\tilde{\sigma}(E_k, E_{k'})$ by values obtained by interpolating between the near-diagonal elements. The resulting correlation coefficient,

$$C(E_k, E_{k'}) \; = \; \tilde{\sigma}_{E_k E_{k'}} / [\tilde{\sigma}_{E_k} \tilde{\sigma}_{E_{k'}}] \; , \qquad (28)$$

is then regular. It is displayed in Fig. 15 for the ensemble obtained for $E_n = 0.5$ MeV by fitting to $\overline{\nu}$ alone. Figure 16 shows cuts at constant total neutron energy, $E_k + E_{k'}$. Similar results are found for all other incident energies considered.

When the model parameters are varied, the spectral shapes tend to pivot around $E \approx 2$ MeV. Consequently, when both neutron energies lie on the same side of this value, the differential changes are in phase and the correlation coefficient is close to one.0 The changes are in opposite directions when the two energy values are on opposite sides of the pivot energy. By contrast, when the spectral data are included in the fits, the correlation coefficients vary widely between $+1$ and -1 in no apparent pattern.

When the number of FREYA events included in the $\overline{\nu}$-only fits at $E_n = 0.5$ MeV is increased by a factor of five, the fitted model parameter values change by less than one standard deviation. When the spectra are also included in the fits, the resulting change in the fitted parameter values increases χ^2_ν from 0.75 to $\approx$15 without significantly improving the spectral fits. Moreover, while the fluctuations in the energy correlation coefficients de-

FIG. 12: (Color online.) Prompt neutron spectra calculated in the laboratory frame as a function of outgoing neutron energy for 0.5 MeV incident neutron energies. The solid curve is obtained by fitting $\overline{\nu}$ alone while the dashed curve is fit to both the spectra and $\overline{\nu}$.
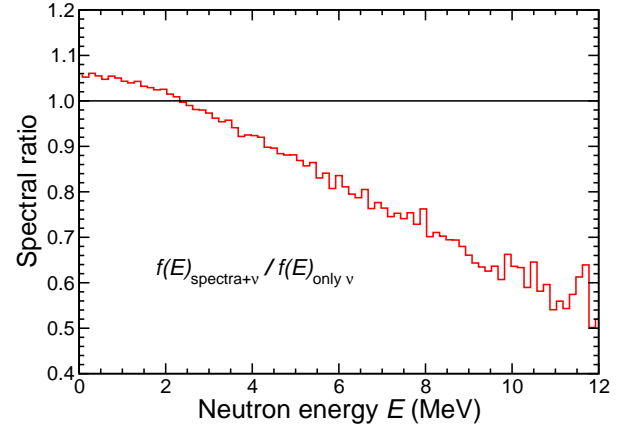
FIG. 13: (Color online.) The ratio of the spectra obtained by fitting to $\overline{\nu}$ *and* the spectral data relative to a fit based on $\overline{\nu}$ alone at $E_n = 0.5$ MeV.

crease somewhat when the larger event samples are used, they do not disappear.

As is the case for the model parameters, there are uncertainties in the spectral calculations. If the model is qualitatively wrong, and the right spectral form cannot be obtained by simply changing the parameter values, then the spectral uncertainties are not correct. To explore this we performed several additional variations on the model. In Sec. IV we saw that a model that employs a constant tip separation d, independent of the specific binary partition, reproduces neither the total kinetic energy data nor the neutron yield as a function of fragment mass. Nevertheless, a constant d_{LH} yields better agreement with the $\overline{\nu}$-only fit in Fig. 12 than with the fit that also includes the spectra. Similarly, making the level density parameter independent of energy, $\tilde{a} = A/e_0$, changes the spectrum by less than 5% at lower energies (< 5 MeV) and by less than 20% at higher energies. Fundamental
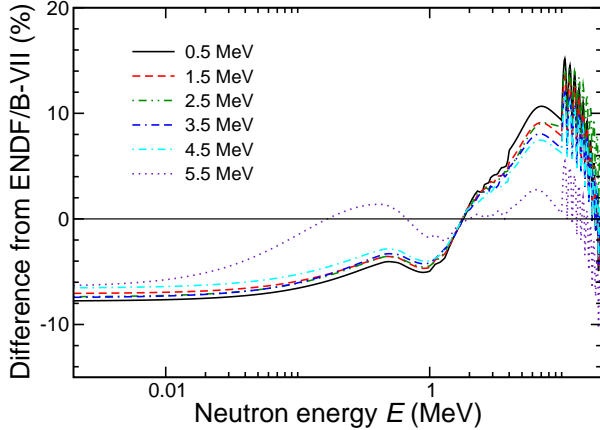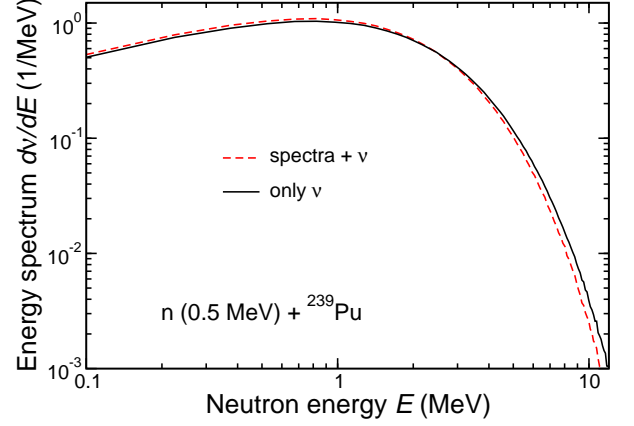

FIG. 11: (Color online.) The percent difference between our evaluated spectra and that of ENDF-B/VII for all six incident neutron energies considered.
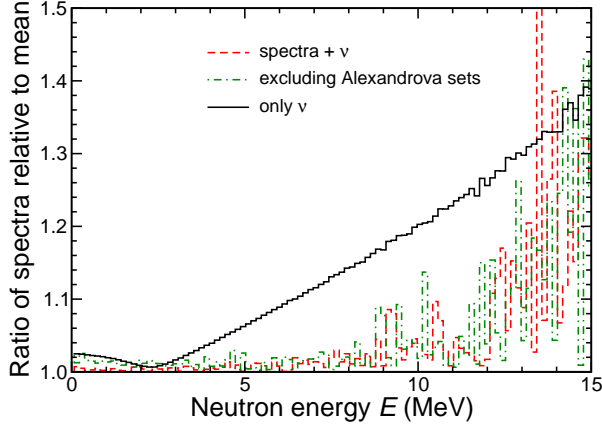
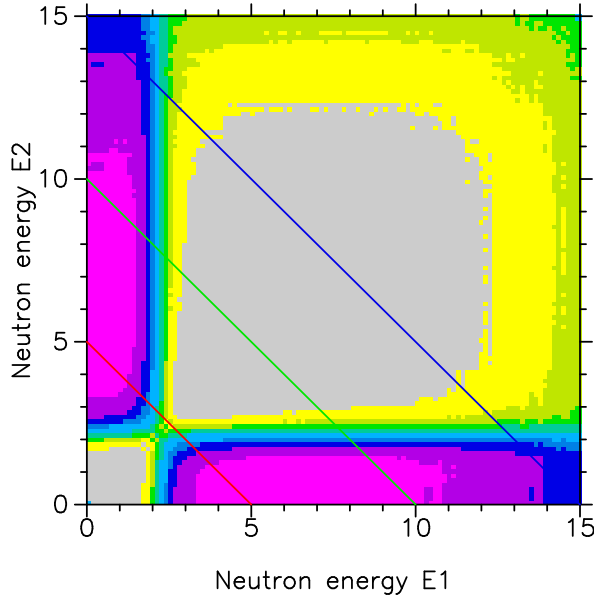FIG. 14: (Color online.) The spectral ratios (see text) for the three different analyses indicated.

FIG. 15: (Color online.) The correlation coefficients, $C(E_1, E_2)$, for the spectral strength of the evaporated neutrons (see Eq. (28)), as obtained from the statistical analysis at $E_n = 0.5$ MeV when only $\overline{\nu}$ is considered in the fits. Figure 16 shows cuts along the three indicated lines of constant total energy.

microscopic calculations of fission could provide insight into the sensitivity of the spectrum to changes in the parameters, leading to better estimates of the spectral uncertainties.

Critical assemblies, which are designed to determine the conditions under which a fission chain reaction is stationary, provide an important quality check on the spectral evaluations. The key measure of a critical assembly is the neutron multiplication factor k_{eff} (often denoted as the k eigenvalue). When this quantity is unity, the assembly is exactly critical, *i.e.* the net number of neutrons resulting from each neutron-induced fission event is one on the average. (This number is the difference between the number of neutrons emitted during the fission process and those lost to absorption and escape.) The degree of criticality of a particular assembly depends on the multiplicity of prompt neutrons, their spectral shape, and the (n, f) induced-fission cross section.

Plutonium criticality is especially sensitive to the prompt neutron spectrum because the ^{239}Pu(n, f) cross section rises sharply between $E_n = 1.5$ and 2 MeV. As a result, increasing the relative number of low-energy neutrons tends to decrease criticality, lowering k_{eff}, while increasing the number of neutrons having higher energy increases criticality.

Figure 17 shows calculations of k_{eff} for different plutonium assemblies. Apart from the spectra, all data used in these calculations were taken from ENDF/B-VII. Overall there is good agreement with the measured values of k_{eff}, though this new softer spectrum decreases the calculated values by about 0.003. Since this is approximately 1.5 standard deviations away from the measurement, there may be an indication that the Pu fission cross section or neutron multiplicity is low by about a tenth of a percent. There appears to be room for some adjustment of the experimental data since the uncertainties in the cross sections are about 1%, while those in $\overline{\nu}$ are about 0.5%.

D. More exclusive observables

Though less important for understanding energy production, more exclusive observables play a central role in the development of a comprehensive description of fission. Figure 18 shows calculations of fragment kinetic and excitation energies. Note that the fragment kinetic energies are almost independent of the incident neutron energy. Indeed, the kinetic energy appears to decrease slightly with energy, as may be expected since s increases. This may at first appear surprising but the Coulomb approximation to the total kinetic energy in Eq. (13) is independent of the incident neutron energy. These results are consistent with measurements made with ^{235}U and ^{238}U targets over a similar incident neutron energy range, $0.5 \leq E_n \leq 6$ MeV [43] and $1.2 \leq E_n \leq 5.8$ MeV
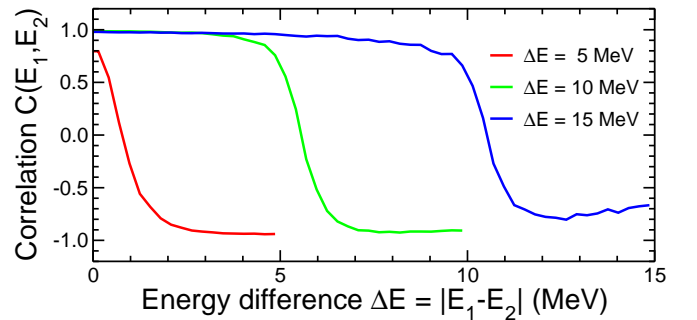

FIG. 16: (Color online.) The spectral correlation coefficients, $C(E_1, E_2)$, along the three lines of constant combined energy indicated in Fig. 15.
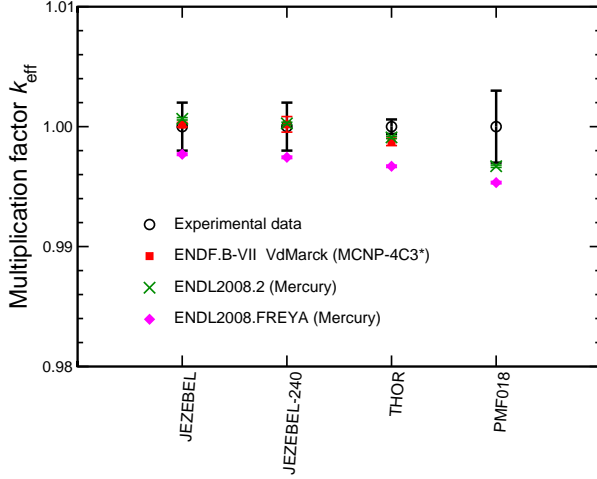
FIG. 17: (Color online.) Calculated k_{eff} for several ^{239}Pu critical assemblies obtained using our fits for $0.5 \leq E_n \leq 5.5$ MeV in the Mercury Monte Carlo. The results are compared to those with the standard ENDL2008.2 and ENDF-B/VII databases.

[44] respectively. In both cases, the average TKE, $\overline{\text{TKE}}$, changes less than 1 MeV over the entire energy range. Ref. [44] also shows that, while the mass-averaged TKE is consistent with near energy independence, higher energy incident neutrons typically give more TKE to masses close to symmetric fission and somewhat less TKE for $A_H > 140$. The slight increase in TKE close to symmetric fission of ^{238}U is not unexpected since the symmetric contribution to $Y(A)$ increases with incident neutron energy. Since such detailed TKE information is not available for neutrons on ^{239}Pu, we have therefore chosen to use a constant scale factor at each energy.

The constancy of the fragment kinetic energy as a function of E_n allows the energy of the incident neutron to be converted into excitation energy. The increase of E^* with E_n is fairly monotonic over all A_f, see the right-hand side of Fig. 18. It appears, however, that the slope of $\nu(A_f)$ for $A_f > 120$ increases somewhat faster with E_n than for $A_f < 120$, as shown on the left-hand side of Fig. 19. This scenario is consistent with washing out the sawtooth pattern of $\nu(A_f)$ with increasing neutron energy [45]. See Table VI for the average neutron multiplicity for the light and heavy fragments as well as the sum. The associated multiplicity dispersions, $\sigma_\nu = [\langle \nu \rangle^2 - \overline{\nu}^2]^{1/2}$, are also given. Since $\overline{\nu}$ is used to determine the values model parameters, it may be preferable to use a different (and more exclusive) observable to check whether a given model parameter set is preferred over another. A better choice is the average neutron multiplicity and average neutron energies from the individual fragments. There are some limited data on thermal neutron-induced fission of ^{235}U [46] and spontaneous fission of ^{252}Cf [47] which suggest that the light fragment emits more neutrons than the heavy fragment, 40% more for ^{235}U [46] and 20% more for ^{252}Cf [47]. Our results for 0.5 MeV,
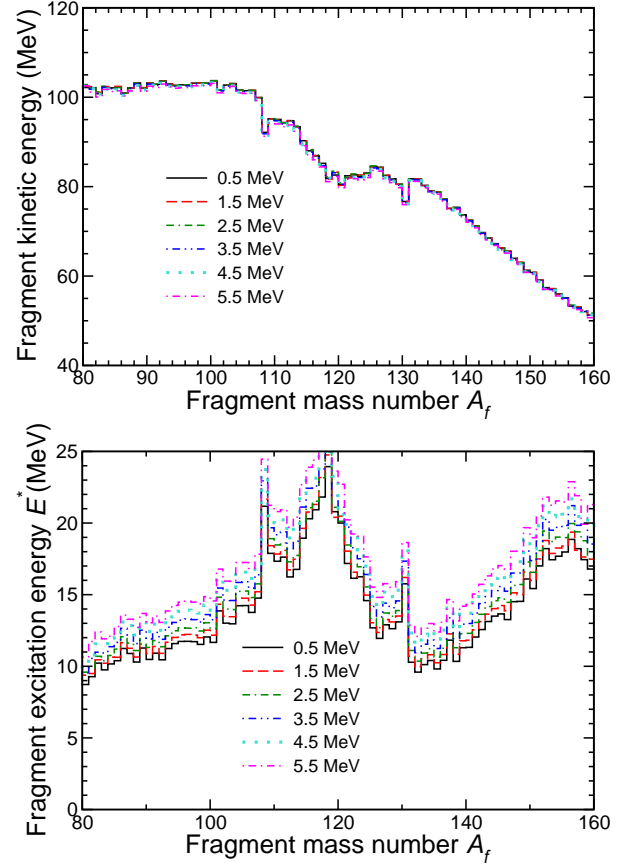

FIG. 18: (Color online.) The average kinetic energy of the fission fragments (*upper panel*) and their average excitation (*lower panel*) as a function of fragment mass number A_f for $0.5 \leq E_n \leq 5.5$ MeV.

shown in Table VI, give a relative difference in $\overline{\nu}$ between the light and heavy fragments of about 20% for $x \sim 1.1$. Fits to $\overline{\nu}$ and the spectral data rather than $\overline{\nu}$ alone give $\overline{\nu}_L \approx \overline{\nu}_H$ for $E_n \leq 0.5$ MeV, seemingly excluded by these measurements, if the same is true for Pu.

A more sensitive neutron observable is the kinetic energy of an evaporated neutron. The lower panel in Fig. 19 shows the average kinetic energies of the emitted neutrons as a function of fragment mass for the lowest and highest incident energies studied (0.5 and 5.5 MeV). The average kinetic energy of the emitted neutrons is almost constant with A except in the region $110 < A < 140$ where it increases. The dip in TKE occurs in the symmetric region, making more energy available for neutron emission, resulting in more and faster prompt neutrons.

In Fig. 20 we show the probability for a given neutron multiplicity, $P(\nu)$, as a function of neutron number for all E_n. Along with the probability distribution for emission from both fragments, we also show the distributions for the light and heavy fragments separately.

Table VII gives the average energies of the neutrons emitted from the light fragment, the heavy fragment, or
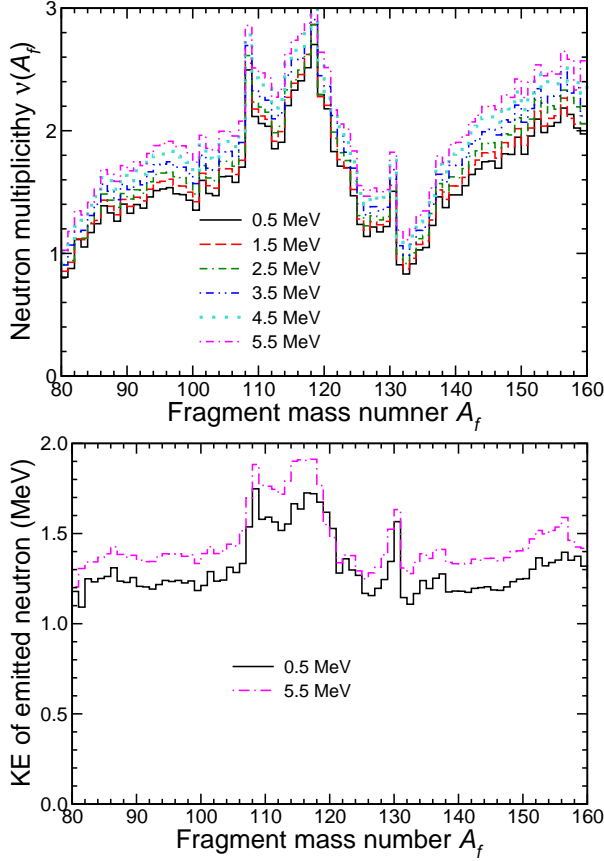
FIG. 19: (Color online.) The average neutron multiplicity for $0.5 \leq E_n \leq 5.5$ MeV (*upper panel*) and the mean kinetic energy of the evaporated neutrons (lower panel) for $E_n = 0.5$ and 5.5 MeV, as functions of the fission fragment mass number A_f.
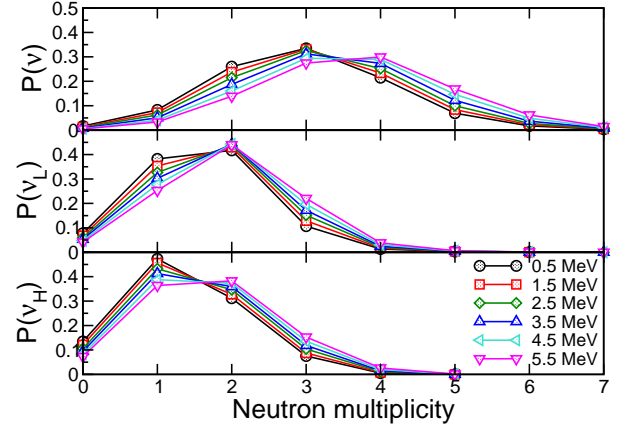

FIG. 20: (Color online.) The normalized neutron multiplicity distribution obtained with FREYA for both fragments (top), the light fragment (middle) and the heavy fragment (bottom). Results are shown for $0.5 \leq E_n \leq 5.5$ MeV.

E_n	$\langle E^{L+H} \rangle$	σ_E^{L+H}	$\langle E^L \rangle$	σ_E^L	$\langle E^H \rangle$	σ_E^H
0.5	2.054	1.625	2.313	1.755	1.750	1.418
1.5	2.088	1.654	2.346	1.787	1.785	1.448
2.5	2.113	1.674	2.369	1.809	1.816	1.474
3.5	2.140	1.698	2.397	1.836	1.828	1.496
4.5	2.168	1.721	2.425	1.860	1.873	1.521
5.5	2.198	1.746	2.455	1.883	1.905	1.546

TABLE VII: The average energy of neutrons emitted by either fragment and by the light and heavy fragments separately, along with the associated dispersions, for various incoming neutron energies (all in MeV).

average energies but increase more slowly with incident energy. The overall average energy $\langle E \rangle$ is similar to that obtained for thermal neutron-induced fission of ^{235}U and ^{252}Cf(sf) found in Ref. [9].

VI. CONCLUSION

Our studies employ the recently developed a Monte-Carlo model, FREYA, that simulates fission and the subsequent neutron and photon emission from the fragments on an event-by-event basis, maintaining energy and momentum conservation at each step in the production and de-excitation of the fragments. We have introduced three adjustable parameters, s, a, and x, which modulate the separation between the tips of the fragments, scale the level-density parameter for the fragments, and modify the partition of energy between them, respectively. These three model parameters were varied over an appropriate range and, for each particular set of values, FREYA was used to generate a large sample of fission events from which the resulting properties of the neutron spectra were extracted. Each set of parameter values was assigned a

from either, together with the associated variances, for the incident neutron energies E_n. The average energies increase with E_n in all cases and those coming from the light fragment tend to be more energetic than those coming from the heavy one, so we have $\langle E^L \rangle > \langle E^{L+H} \rangle > \langle E^H \rangle$. The variances exhibit the same hierarchy as the

E_n (MeV)	$\overline{\nu}$	$\sigma_{\overline{\nu}}$	$\overline{\nu}_L$	$\sigma_{\overline{\nu}_L}$	$\overline{\nu}_H$	$\sigma_{\overline{\nu}_H}$
0.5	2.947	1.381	1.604	0.723	1.343	0.676
1.5	3.090	1.400	1.685	0.755	1.405	0.704
2.5	3.244	1.424	1.761	0.783	1.483	0.738
3.5	3.376	1.443	1.828	0.806	1.548	0.767
4.5	3.530	1.466	1.905	0.833	1.624	0.801
5.5	3.683	1.499	1.983	0.863	1.699	0.836

TABLE VI: The mean combined neutron multiplicities $\overline{\nu}$ as well as the mean multiplicities of neutrons emitted from either the light or the heavy fragment, $\overline{\nu}_L$ and $\overline{\nu}_H$, together with the associated dispersions.

likelihood weight based on the χ^2 obtained from comparison with the measured mean multiplicity $\overline{\nu}$ and/or the measured differential neutron spectrum $d\overline{\nu}/dE$. Mean values and covariances for both input parameters and quantities predicted by the model were obtained through standard statistical techniques. This combination of the Monte-Carlo fission model with the likelihood weighting presents a powerful tool for the evaluation of fission-neutron data.

This procedure was applied to the analysis of neutron-emission data for neutron-induced fission on ^{239}Pu, from thermal to 5.5 MeV incident energies. Although the approach taken and the nucleus studied in this work are different, the results largely corroborate the findings of Lemaire *et al.* [9] in emphasizing the importance of the initial conditions (*e.g.* the kinetic and excitation energies of the fragments). Furthermore, our work underscores the effectiveness of the measured $\overline{\nu}$ in constraining the model parameters, more strongly even than the differential neutron-spectrum data. In particular, it was found the the parameter controlling the tip separation between fragments was by far the most important in reproducing the experimental $\overline{\nu}$ values. In the end, fits of our model to the $\overline{\nu}$ data alone (*i.e.*, excluding the differential-spectral data) were found to be more robust and were used to obtain the best model parameters.

We plan to apply this method to the prediction of neutron emission properties in other actinides. However, in those cases where critical experimental data (such as kinetic energies and neutron multiplicities and spectra) are not available to constrain the FREYA calculations, it may be necessary to invoke supplementary information from various theoretical models, such as Hartree-Fock-Bogoliubov or macroscopic-microscopic treatments.

[1] N. Bohr and J.A. Wheeler, Phys. Rev. **56**, 426 (1939).
[2] O. Hahn and F. Strassmann, Naturwissenschaften **27**, 11 (1939).
[3] L. Meitner and O.R. Frisch, Nature **143**, 239 (1939).
[4] P. Möller, D.G. Madland, A.J. Sierk, and A. Iwamoto, Nature **409**, 785 (2001).
[5] P. Möller, A.J. Sierk, T. Ichikawa, A. Iwamoto, R. Bengtsson, H. Uhrenholt, and S. Åberg, Phys. Rev. C **79**, 064304 (2009).
[6] J.-F. Berger, M. Girod, and D. Gogny, Nucl. Phys. A **428**, 23 (1984).
[7] H. Goutte, J.-F. Berger, P. Casoli, and D Gogny, Phys. Rev. C **71**, 024316 (2005).
[8] N. Dubray, H. Goutte, and J.-P. Delaroche, Phys. Rev. C **77**, 014310 (2008).
[9] S. Lemaire, P. Talou, T. Kawano, M.B. Chadwick, and D.G. Madland, Phys. Rev. C **72**, 024601 (2005).
[10] H. Conde, J. Hansen, and M. Holmberg, J. Nucl. Energy **22**, 53 (1968): http://www-nds.iaea.org/exfor/servlet/X4sGetSubent?subID=20052002.
[11] J. Frehaut, G. Mosinski, and M. Soleilhac, private communication (1980): http://www-nds.iaea.org/exfor/servlet/X4sGetSubent?subID=20490003.
[12] B. Nurpeisov *et al.*, Atom. Ener. **39**, 199 (1975): http://www-nds.iaea.org/exfor/servlet/X4sGetSubent?subID=40429004.
[13] J.W. Boldeman, and R.L. Walsh, J. Nucl. Energy **25**, 321 (1971): http://www-nds.iaea.org/exfor/servlet/X4sGetSubent?subID=30006004.
[14] J.C. Hopkins and B.C. Diven, Nucl. Phys. A **48**, 433 (1963): http://www-nds.iaea.org/exfor/servlet/X4sGetSubent?subID=12326006.
[15] E. Fort, J. Frehaut, H. Tellner, and P. Long, Nucl. Sci. Eng. **99** (1988) 375.
[16] M.B. Chadwick *et al.*, Nuclear Data Sheets **107** (2006) 2931.
[17] H. Conde and G. During, Arkiv för Fysik **29**, 313 (1965): http://www-nds.iaea.org/exfor/servlet/X4sGetSubent?subID=20575006.
[18] L.M. Belov, M.V. Blinov, N.M. Kazarinov, A.S. Krivokhatskij, and A.N. Protopopov, Yad.-Fiz. Issl. Rep. **6**, 94 (1968): http://www-nds.iaea.org/exfor/servlet/X4sGetSubent?subID=40137004.
[19] H. Knitter, Atomkernenerg. **26**, 76 (1975): http://www-nds.iaea.org/exfor/servlet/X4sGetSubent?subID=20576003.
[20] Z.A. Aleksandrova, V.I. Bol Shov, V.F. Kuznetsov, G.N. Smirenkin, and M.Z. Tarasko, Atom. Energ. **38**, 108 (1975): http://www-nds.iaea.org/exfor/servlet/X4sGetSubent?subID=40358002; http://www-nds.iaea.org/exfor/servlet/X4sGetSubent?subID=40358003.
[21] D. Abramson and C. Lavelaine, A.E.R.E. Harwell Rep. No. 8636 (1977):

http://www-nds.iaea.org/exfor/servlet/X4sGetSubent?subID=20997004.

[22] V. N. Nefedov, B. I. Starostov, and A. A. Bojcov, "6th All-Union Conf. on Neutron Physics", Kiev, Ukraine (1983) Vol. 2, p. 285: http://www-nds.iaea.org/exfor/servlet/X4sGetSubent?subID=40871009.

[23] P. Staples, J.J. Egan, G.H.R. Kegel, A. Mittler, and M.L. Woodring, Nucl. Phys. A **591**, 41 (1995): http://www-nds.iaea.org/exfor/servlet/X4sGetSubent?subID=13982003.

[24] H. Werle and H. Bluhm, "Prompt Fission Neutron Spectra Meeting", Vienna, Austria (1971) p. 65: http://www-nds.iaea.org/exfor/servlet/X4sGetSubent?subID=20616005.

[25] B. I. Starostov, V. N. Nefedov, and A. A. Bojcov, "6th All-Union Conf. on Neutron Physics", Kiev, Ukraine (1983) Vol. 2, p. 290: http://www-nds.iaea.org/exfor/servlet/X4sGetSubent?subID=40872003.

[26] C. Wagemans, E. Allaert, A. Deruytter, R. Barthélémy, and P. Schillebeeckx, Phys. Rev. C **30**, 218 (1984): http://www-nds.iaea.org/exfor/servlet/X4sGetSubent?subID=21995038.

[27] K. Nishio, Y. Nakagome, I. Kanno, and I. Kimura, J. Nucl. Sci. Technol. **32**, 404 (1995): http://www-nds.iaea.org/exfor/servlet/X4sGetSubent?subID=23012006; http://www-nds.iaea.org/exfor/servlet/X4sGetSubent?subID=23012005.

[28] C. Tsuchiya, Y. Nakagome, H. Yamana, H. Moriyama, K. Nishio, I. Kanno, K. Shin, and I. Kimura, J. Nucl. Sci. Technol. **37**, 941 (2000): http://www-nds.iaea.org/exfor/servlet/X4sGetSubent?subID=22650003: http://www-nds.iaea.org/exfor/servlet/X4sGetSubent?subID=22650005.

[29] J. Randrup and R. Vogt, Phys. Rev. C, in press, arXiv:0906.1250 [nucl-th], LLNL-JRNL-413625 (2009).

[30] A. Tarantola, "Inverse Problem Theory", SIAM press (2005).

[31] T. R. England and B. F. Rider, LA-UR-94-3106 (1994).

[32] W. Reisdorf, J.P. Unik, H.C. Griffin, and L.E. Glendenin, Nucl. Phys. A **177** (1971) 337.

[33] U. Brosa, S. Grossmann, and A. Müller, Phys. Rep. **97**, 1 (1990); U. Brosa, Phys. Rev. C **32**, 1438 (1985).

[34] F.-J. Hambsch, H. H. Knitter, C. Budtz-Jørgensen, and J. P.Theobald, Nucl. Phys. A **491**, 56 (1989).

[35] G. Audi and A.H. Wapstra, Nucl. Phys. A **595**, 409 (1995).

[36] P. Möller, J.R. Nix, W.D. Myers, and W.J. Swiatecki, At. Data Nucl. Data Tab. **59**, 185 (1995).

[37] V.F Apalin, Yu.N. Gritsyuk, I.E. Kutikov, V.I. Lebedev, and L.A. Mikaelian, Nucl. Phys. A **71**, 553 (1965): http://www-nds.iaea.org/exfor/servlet/X4sGetSubent?subID=41397002.

[38] T. Kawano, private communication.

[39] H. Koura, M. Uno, T. Tachibana and M. Yamada, Nucl. Phys. A **674**, 47 (2000).

[40] V.F. Weisskopf, Phys. Rev. **52**, 295 (1937).

[41] P. R. Bevington and D. K. Robinson, "Data Reduction and Error Analysis for the Physical Sciences", 2nd ed., McGraw-Hill, Inc. (1992).

[42] G.F. Burgio, Ph. Chomaz, and J. Randrup, Nucl. Phys. A **529**, 157 (1991).

[43] F.-J. Hambsch, private communication (2008).

[44] F. Vivès, F.-J. Hambsch, H. Bax, and S. Oberstedt, Nucl. Phys. A **662**, 63 (2000).

[45] R. Vandenbosch and J.R. Huizenga, "Nuclear Fission", Academic Press (1973).

[46] K. Nishio, Y. Nakagome, H. Yamamoto and I. Kimura, Nucl. Phys. A **632**, 540 (1998).

[47] A.S. Vorobyev, V.N. Dushin, F.J. Hambsch, V.A. Jakovlev, V.A. Kalinin, A.B. Laptev, B.F. Petrov, and O.A. Shcherbakov, "Proc. of the Intl. Conf. on Nuclear Data for Science and Technology", ND2004, Santa Fe, NM, USA (2004).